Synthesis of water-stable and highly luminescent graphite quantum dots

Slavia Deeksha Dsouza[1,2] ⓘ, **Marius Buerkle**[1] ⓘ, **Bruno Alessi**[2] ⓘ,
Paul Brunet[2] ⓘ, **Alessio Morelli**[2] ⓘ, **Amir Farokh Payam**[2] ⓘ, **Paul Maguire**[2] ⓘ,
Davide Mariotti[2] ⓘ and **Vladimir Svrcek**[1] ⓘ

[1] National Institute of Advanced Industrial Science and Technology (AIST) Central 2, Umezono 1-1-1, Tsukuba, Ibaraki, 305-8568, Japan
[2] School of Engineering, Ulster University, Belfast, BT15 1AP, United Kingdom

E-mail: d.mariotti@ulster.ac.uk

CrossMark

Abstract

Highly stable and environmentally friendly nitrogen-doped graphite quantum dots consisting of ~12 layers of graphene, average diameter of ~7.3 nm, prepared by atmospheric pressure microplasma are reported to have blue emission due to surface states created by nitrogen doping (9 atomic%) and reaction with oxygen. The low-temperature synthesis method requires simple precursors in water, with no annealing or filtration, producing crystalline disc-shaped quantum dots with ~68% photoluminescence emission quantum yield at 420 nm excitation and that have shown stability for more than one month after the synthesis. The nitrogen doping in the quantum dots mainly occurs in graphitic core as substituted type of doping (63–67 atomic%) and the amount of doping is sufficient to create emissive states without impacting the core structure. The optical and chemical properties do not undergo serious retardation even with re-dispersion suggesting easy applicability for cellular imaging or optoelectronics.

Supplementary material for this article is available online

Keywords: colloids, doping, electro-optical materials, blue luminescence, atmospheric pressure microplasma

(Some figures may appear in colour only in the online journal)

Introduction

Luminescent nanomaterials have gained great attention among researchers in the past few years due to various applications in biological sensing, imaging and optoelectronics [1–5]. Many of the photoluminescent nanomaterials are semiconductors and usually contain toxic elements, heavy and expensive metals which have limited their applications. Carbon nanoparticles are a promising alternative to semiconductor nanocrystals as next generation green nanomaterials due to excellent biocompatibility, low cytotoxicity and solution processability which results in ease of production and incorporation in devices [6]. Since their discovery [7], immense improvements in their luminescent properties and synthesis methods have been achieved (table S1, supporting information). Carbon nanoparticles with diameters below 10 nm that are exhibiting quantum confinement are generally classified as graphene quantum dots (crystalline graphene with single or few graphene layers, usually <5), carbon or graphite quantum dots (several graphene layers) or carbon nanodots (amorphous carbon) [8–10]. Carbon quantum dots (CQDs) have in general a large surface area and, due to dense surface groups, could be considered as a carbon core–shell nanostructure. The carboxyl and hydroxyl groups at the surface impart high solubility in water and assist in surface functionalization with other polymers, organic molecules or biological species [6].

Xu *et al* have found that doping CQDs with nitrogen enhances the luminescence properties by creating emissive energy traps in the carbon hexagonal rings [11]. Nitrogen has been widely employed as a doping agent due to comparable atomic size as carbon. Without the presence of nitrogen dopant, the carboxylic and epoxy groups that are present on the carbon dot surface enhance non-radiative recombination by decreasing the density of π-electrons. Due to nitrogen containing precursor, such functional groups could transform to amide groups which have strong electron donating property and thus radiative recombination increases, leading to a higher photoluminescence quantum yield (PLQY) [12]. Thus, the PLQY is largely dependent on the synthesis condition and resulting chemical structure. Several reports deal with surface modification and post-synthesis approaches to increase PLQY and the highest achieved till date is 100% by Das *et al* using non-toxic precursors at high temperature [13]. Other high PLQY CQDs have been achieved by high-temperature synthesis methods, lengthy reaction times, post-synthesis treatments like purification, chromatography, and functionalization [14–20].

Synthesis method used for CQDs should be carefully chosen because integration into devices for applications requires non-agglomerated CQDs and the process should be relatively easy and environmentally friendly. Low temperature atmospheric pressure microplasmas offer a one-step easy and non-toxic method for the synthesis of CQDs and also allow for controlling the optical and electronic properties by changing the experimental parameters [21, 22]. Microplasma-based methods have been explored to synthesize CQDs to accelerate chemical reactions causing carbonization of precursors. Although the PLQY of the resulting CQDs was considerably low (maximum 9.9% by Ma *et al* [23]), surface functionalization presents some advantages as it can be carried out in a single step during synthesis and not as a separate post-synthesis treatment. The study by Huang *et al* showed that CQDs produced by microplasma illustrated enhanced luminescence compared with chemical-based heating method [24]. In the current work we have used a 30 min one-step microplasma process to obtain stable, non-toxic, re-dispersible, excitation-dependent photoluminescent nitrogen-doped graphite quantum dots (N-GQDs) with highest photoluminescence QY obtained using this synthesis method and have suitable optical characteristics for potential applications in biological imaging and solar cells. For these N-GQDs to be used in the fabrication of thin films for applications, it is often required to purify the particles and re-disperse them in different solvents, which are suitable for the deposition technique (e.g. spray coating, spin coating etc). This may require drying in air where atmospheric humidity/moisture could cause changes in the chemical structure and subsequently change in the optical properties. In this study, we have effectively shown the stability of the synthesized N-GQDs even when subjected to more demanding conditions, such as re-dispersion in water.

Experimental details

Similar to our previous work [25, 26], a direct-current (DC) atmospheric pressure microplasma is generated and sustained in contact with a solution. In this case the solution contains 0.35 g of succinic acid (SA) and 0.25 g of 1,7-diaminoheptane (DAH) dissolved in 10 ml de-ionized water (15 MΩ cm). The schematic and photograph of the synthesis setup is shown in figure S1 (supporting information). We use here long-chain precursors as they have been reported in the literature to result in increased photostability of carbon dots [27]. The microplasma process is applied for 30 min and a constant discharge current of 4 mA was maintained. At the end of the synthesis, a light-yellow coloured solution is obtained indicating the formation of the nanoparticles. The synthesized N-GQDs were then transferred to a petri-dish and left to dry overnight in the ambient. The dried powder is then re-dispersed in 10 ml of de-ionized water and used for further characterization. The N-GQDs appear to be dispersed in water with no agglomeration or sedimentation. Our results therefore relate to N-GQDs that are characterized as-prepared (AP) from the solution used for the synthesis and N-GQDs after being re-dispersed (RD) in water.

The structure, size, and shape of the N-GQDs are studied using JEOL JEM-2100F transmission electron microscope (TEM) at an accelerating voltage of 200 kV. The samples are prepared by drop-casting the AP N-GQDs onto lacey carbon and graphene oxide grids. Atomic force microscopy (AFM) characterization was performed in air using a commercial system (D3100 Nanoscope III Digital Instruments, now Bruker) in amplitude modulation AFM (tapping mode). Topographic images were acquired at a scan rate of 1 Hz, with a silicon probe for soft tapping mode (FMV-A Bruker, spring constant 3 Nm^{-1}, resonance frequency 75 kHz, radius of curvature 10 nm). Samples for AFM were prepared by dip-coating 12 mm mica substrates in the AP N-GQDs colloid. Fourier transform infrared spectroscopy (FTIR) was carried out using Perkin Elmer FTIR Spectrometer 2000 for AP and RD N-GQDs drop-casted and dried on cleaned Si substrates. Raman spectra of the N-GQDs were measured in ambient atmosphere using Renishaw inVia Confocal Raman Microscope with a 532 nm laser equipped with 20$\times$ objective lens. The samples for the analysis are prepared by spray-coating the N-GQDs on silicon substrates. The measurements were performed in a cycle of 5 sweeps of 10 s each with nominal laser power of 5 mW on the area of the sample under test. To study the chemical composition of the AP and RD N-GQDs, x-ray photoelectron spectroscopy (XPS) was carried out using ESCALAB 250 Xi microprobe spectrometer (ThermoFisher Scientific). The N-GQDs are drop-casted from the colloid onto gold-coated silicon substrates and left to dry overnight before the measurement. The silicon substrates have gold strips deposited by e-beam evaporation which we use for charge correction. The spectra obtained were charge corrected using Au core level and valence band spectra. The XPS survey spectra is recorded with 1 eV step size and 150 eV pass energy, and the narrow scans were recorded with a step size of 0.1 eV and a pass energy of 20 eV. This pass energy
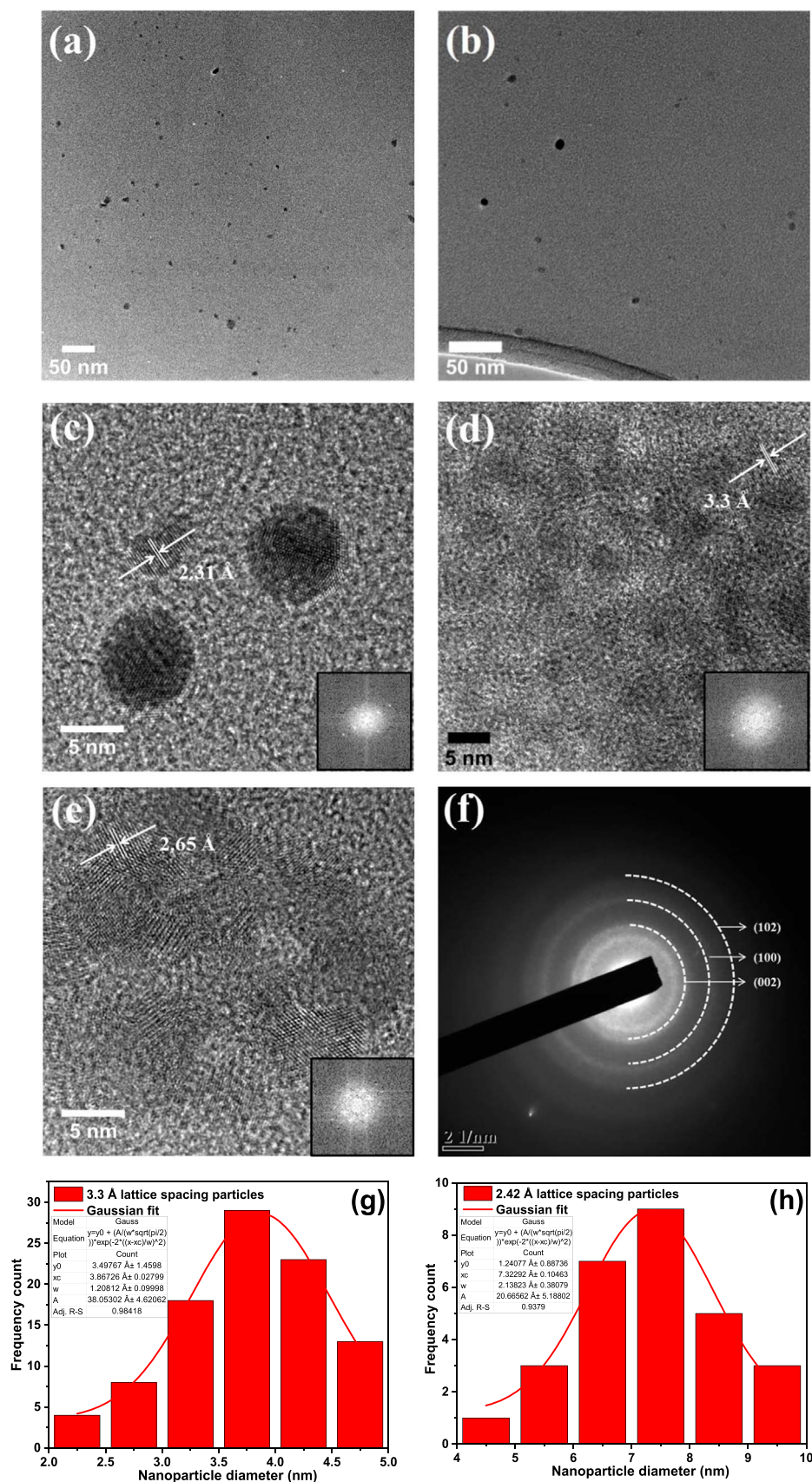
Figure 1. (a) and (b) TEM image of as prepared N-GQDs; (c)–(e) HRTEM image with lattice spacing (insets: FFT of the N-GQDs); (d) SAED pattern of the N-GQDs; (g) particle size histogram when graphene planes orient closer to the perpendicular plane to the grid; (h) particle size histogram when graphene planes orient closer to being parallel to the plane of the grid.
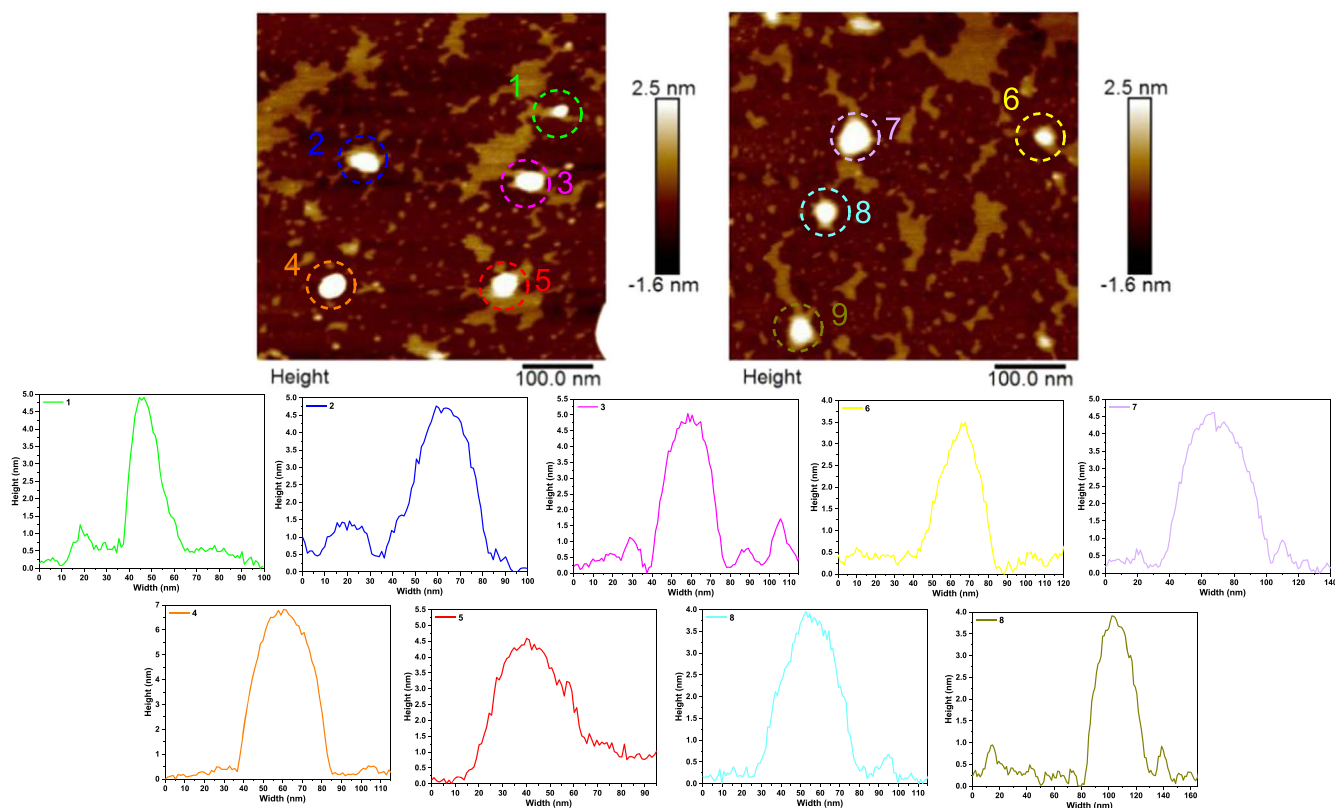
Figure 2. AFM images of the N-GQDs on mica substrates: topography and line profiles of labelled N-CQDs.

gives a 0.65 eV width for the Ag $3d_{5/2}$ peak measured on a sputter cleaned Ag sample. Data analysis and fitting were performed with Thermo Avantage software. After smart background subtraction, components in C 1s and N 1s core level spectra were adjusted using line shapes consisting of convolution products of a Gaussian (70%) function and a Lorentzian (30%) function. The optical properties of the N-GQDs were explored using ultraviolet-visible (UV–vis) absorbance and photoluminescence (PL) spectroscopy. For both measurements, the colloid samples were taken in a 10 mm path length quartz cuvette. For the UV–vis spectra, absorbance of the colloidal samples was measured soon after synthesis with a Perkin Elmer 950 in transmission mode with deionized water as reference for 100% transmission. Photoluminescence (PL) measurements were performed of the colloid in a quartz cuvette with 10 mm path length using Agilent Technologies Cary Eclipse Fluorescence Spectrophotometer G9800A. The excitation area is maintained same by using a mask of 1 cm^2 in the cuvette holder. For absolute quantum yield measurements, an integration sphere attached to a Horiba Jobin Yvon fluoromax-4 spectrometer was used to collect the PL of the N-CQDs. For excitation, a Xe lamp with a double monochromator was used, and the PL was detected by a charge coupled detector (CCD) mounted on a spectrograph via coupled ultraviolet-grade optical fiber. The excitation wavelength was selected through the monochromator. The emission spectra from N-CQDs colloid in a quartz cuvette and the reference were measured, and the number of emitted photons was then calculated from spectral integration. The number of absorbed photons was calculated using reduction of the excitation spectrum and comparing the sample and reference. The absolute PLQY is obtained as the ratio of the number of emitted photons to the number of absorbed photons. Measurements were performed in triplicates and the average value is reported for each excitation wavelength.

Results and discussion

Transmission electron microscopy (TEM) was performed by drop-casting the AP N-GQDs onto lacey carbon and graphene oxide grids. Representative TEM images of the N-GQDs are shown in figures 1(a) and (b). High-resolution TEM (HR-TEM) imaging was used to confirm the crystallinity of the synthesized N-GQDs. Figures 1(c)–(e) show the crystalline phase of the quantum dots. The lattice spacing calculated using fast Fourier transform (FFT), given as insets, was found to be about 3.3 Å, 2.31 Å and 2.65 Å. The first corresponds to the (002) plane spacing reported for graphite (3.3 Å) while the other are close to 2.42 Å, (1120) lattice plane of graphene [28]. This could suggest that the synthesized N-GQDs have different orientations on the grid i.e. sometimes they may orient with the graphene planes closer to the perpendicular plane to the grid and sometimes with graphene planes more parallel to the plane of the grid. This implies that in some cases the (002) plane is clearer to observe and in some other cases the (1120) plane is more obvious. The selected area
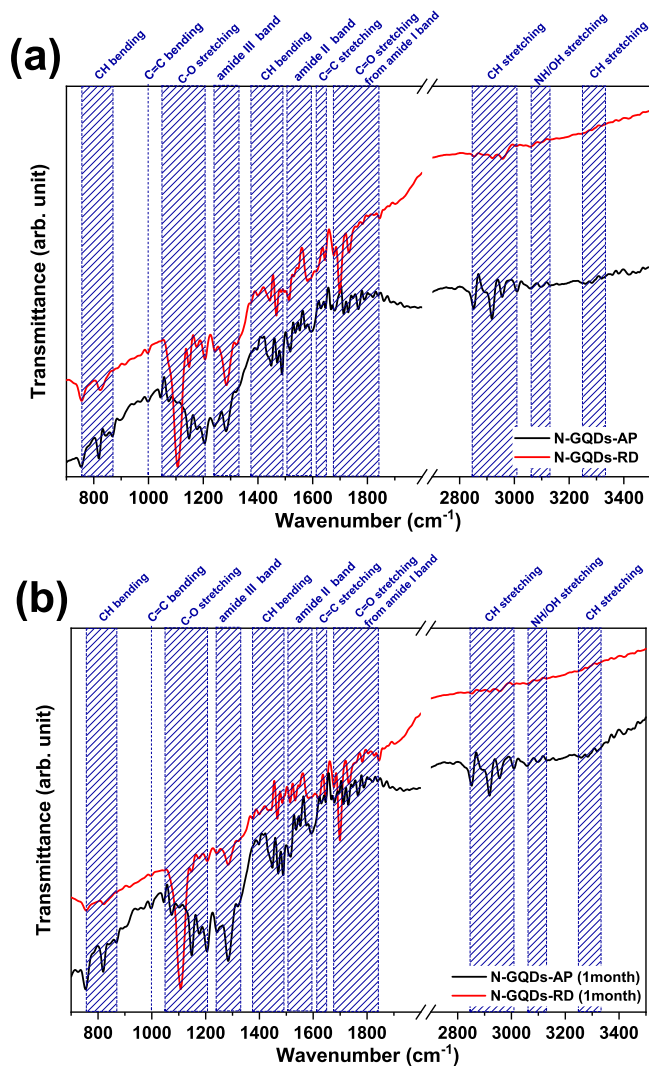
(a)

(b)

Figure 3. FTIR spectra of N-GQDs (a) soon after synthesis and (b) after one month of synthesis.

Figure 4. Raman spectra of as prepared and re-dispersed N-GQDs dried on Si substrates.

diffraction (SAED) pattern rings as shown in figure 1(f) can be indexed to (002), (100) and (102) crystallographic planes of graphite. The histograms of particle sizes depending on the lattice orientation are given in figures 1(g) and (h). It is clear from the histograms that the particles are larger when graphene planes orient parallel to the grid (average size 7.3 nm) and the particles are smaller when graphene planes orient perpendicular to the surface (average size 3.9 nm). We should further note that the orientation with graphene planes perpendicular to the surface was observed only when a degree of agglomeration was noticed; for instance, in figure 1(d) an amorphous matrix (possibly due to the process by-products) seems to hold a number of N-GQDs together and that N-GQDs have therefore the tendency to appear with graphene planes parallel to the grid when non-agglomerated (e.g. figure 1(c)). This suggests that the particles are in fact small discs with average thickness of $\sim$3.9 nm corresponding to an average of $\sim$12 layers of graphene and an average diameter of $\sim$7.3 nm.

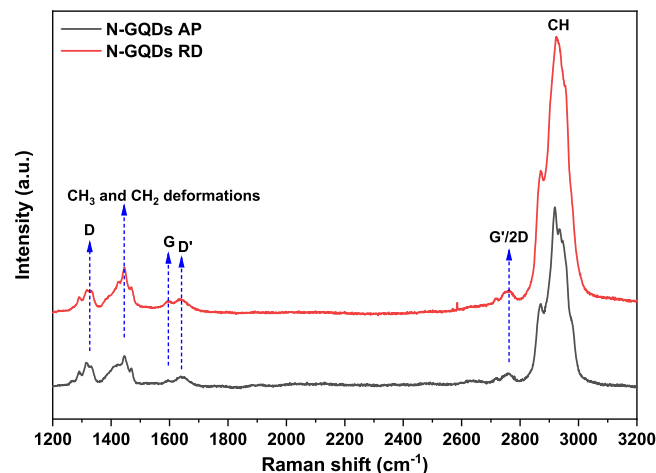To further analyze the morphology of the N-GQDs, atomic force microscopy (AFM) was performed. The mean

height calculated by analyzing the N-GQDs from figure 2 was about 3.6 nm from average of 17 measurements which is well in agreement with the disc thickness distribution obtained by TEM. From these results (figure 1(g) specifically) we can infer that these N-GQDs are formed by 6–15 layers of graphene.

In order to analyse the chemical structure of the N-GQDs and the surface groups, Fourier transform infrared spectroscopy (FTIR) was carried out for AP and RD N-GQDs. The spectra obtained for AP and RD samples are given in figure 3(a). Absorption peaks due to C–H bending vibrations are observed in the range 750–870 cm^{-1} and 1390–1490 cm^{-1} [29] along with C–H stretching vibrations at 2850–3000 cm^{-1} [30]; as these appear to be stronger in the AP sample, these results could suggest incomplete carbonization of precursors [31]. The other absorption bands are C–O stretching at 1070–1200 cm^{-1} [29], amide-III band at 1250–1330 cm^{-1} consisting of mostly N–H bending and C–N stretching [32], amide-II band at 1500–1600 cm^{-1} [32], C=C stretching at 1610–1650 cm^{-1} [25, 29], C=O stretching from amide-I band at 1680–1830 cm^{-1} [30, 32] and N–H or O–H stretching at 3060–3130 cm^{-1} [30]. CH stretching and bending vibrations are stronger from AP N-GQDs and could suggest that AP N-GQDs are mainly hydrogen terminated as opposed to RD N-GQDs which have mainly C–O–C (epoxy) and O=C–NH$_2$ (amide) groups on the surface. The stronger presence of C–O/C=O groups in the N-GQDs after redispersion suggests partial oxidation of the carbon discs surface possibly due to drying of the samples in air. The measurement is then repeated for the same N-GQDs after one month and the spectra are given in figure 3(b). After one month, the spectra remain mostly unchanged and confirm a stable chemical structure. The only changes we could observe relate to the increase of some of the peaks due to further minor oxidation in the RD N-GQDs sample or slow reactions with remaining precursor molecules for the AP N-GQDs.

The Raman spectra of the AP and RD N-GQDs are given in figure 4 and similar peaks are obtained for both N-GQDs. The D-band peak at 1320 cm^{-1} indicates the presence of
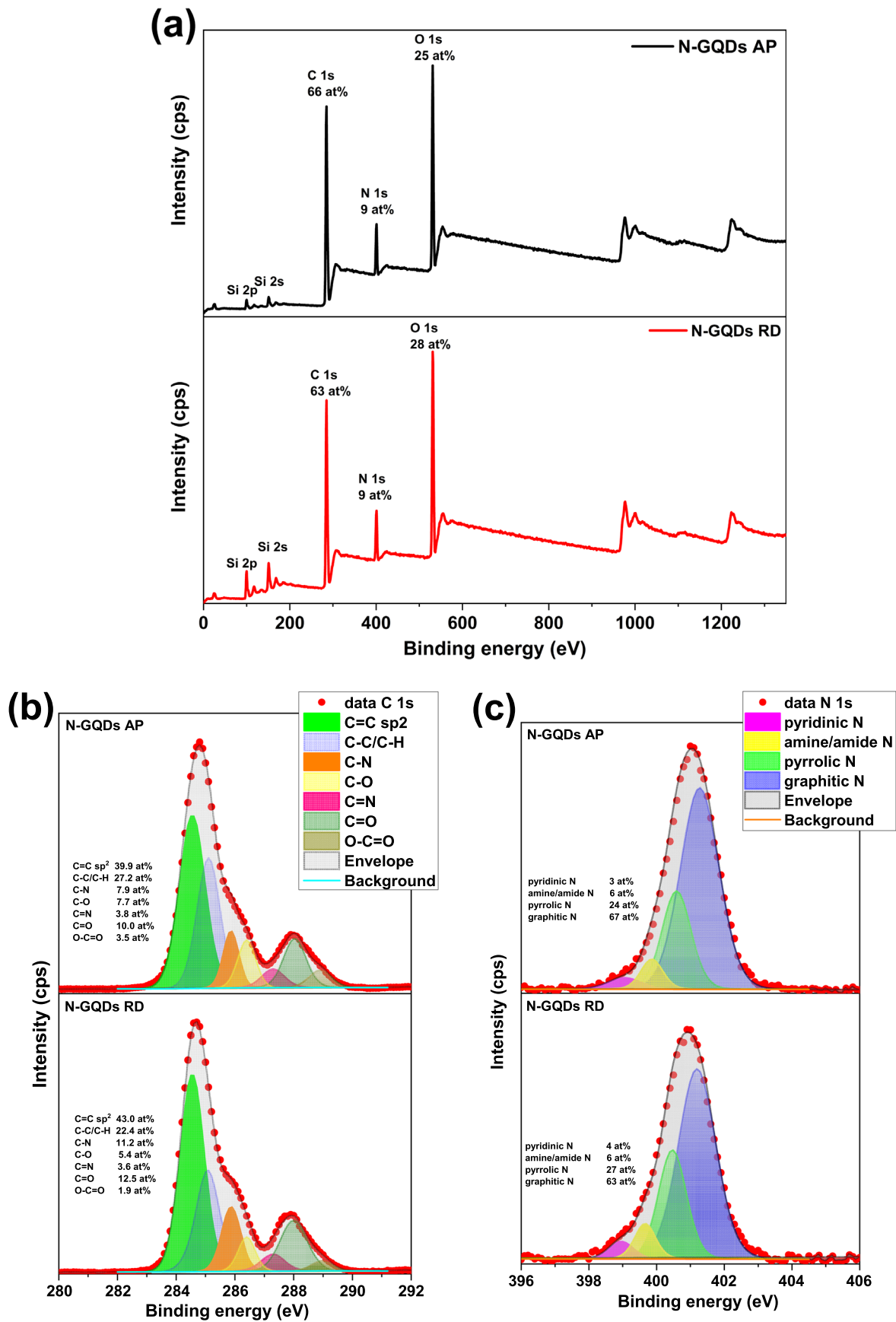
Figure 5. (a) XPS survey spectra of the AP and RD N-GQDs; High resolution XPS scan of (a) C 1s region and (b) N 1s region of AP and RD N-GQDs showing the atomic percentages of components.
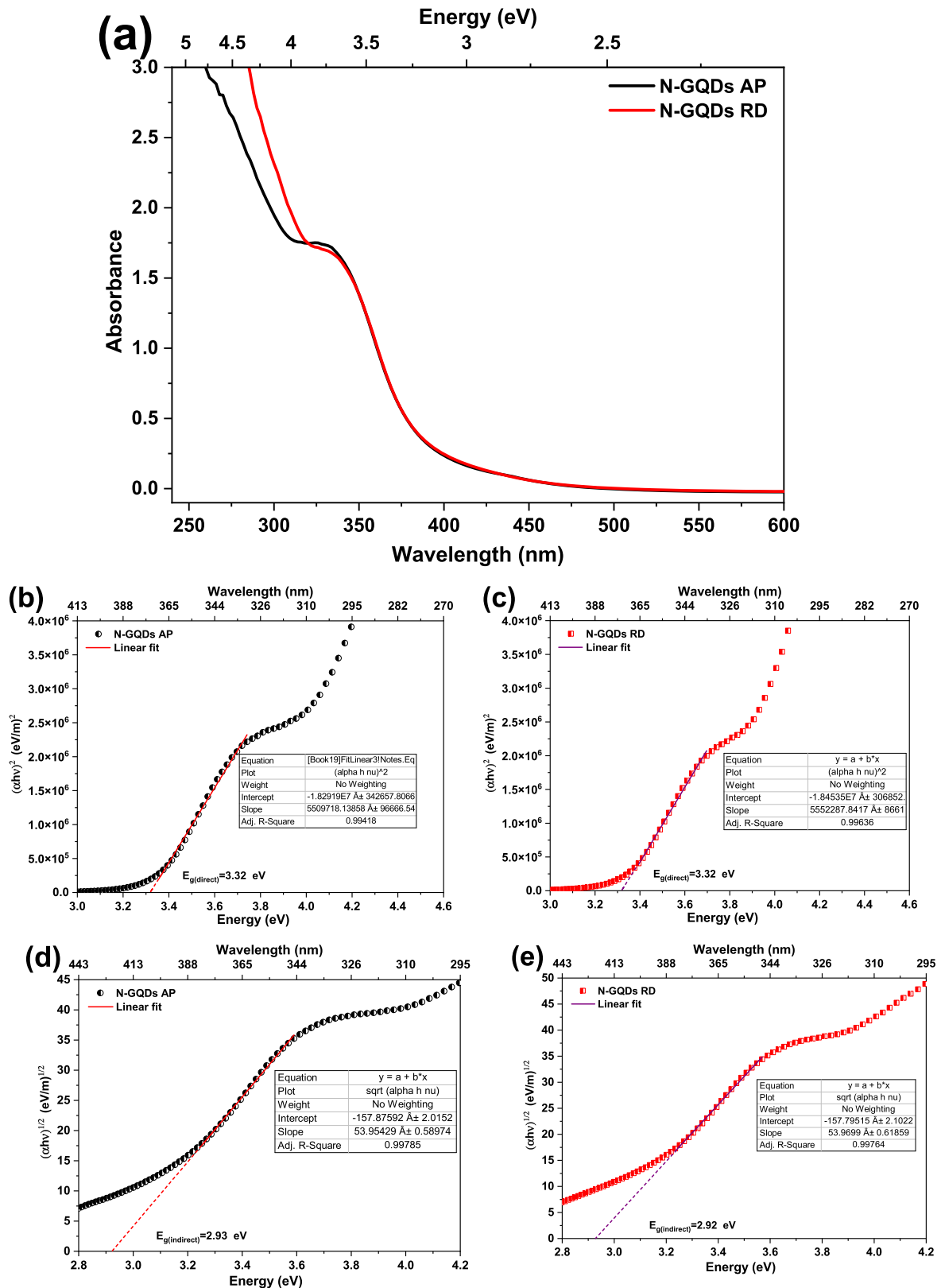
Figure 6. (a) Absorbance spectra of AP and RD N-GQDs; Tauc plots showing direct bandgap of (b) AP and (c) RD N-GQDs; indirect bandgap of (d) AP and (e) RD N-GQDs in colloid.

defects in carbon with sp^2 hybridization which results in loss of translational symmetry at boundaries and interfaces. The D-band arises due to the disruption of the sp^2 hybridized

carbon network. The defects introduce structural irregularities, which affect the electron delocalization and bonding in the quantum dots [33, 34]. The peak at 1448 cm^{-1} can be
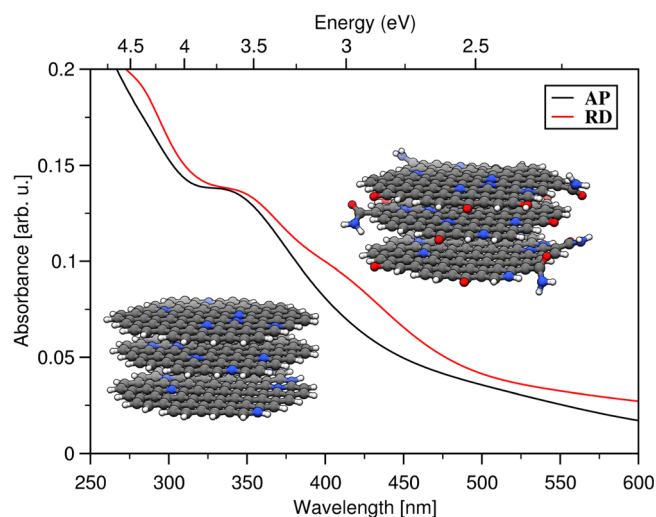
Figure 7. Calculated absorbance spectra for GQDs with hydrogen edge termination (AP), and partially oxidized edges (RD). (Inset particle geometry with C (gray spheres), O (red spheres), N (blue spheres), and H (white spheres).

assigned to CH_3 and CH_2 deformations. The position and intensity of the G-band peak provide valuable information about the crystallinity and purity of quantum dots [35]. In our observations, we have noticed a relatively low intensity due to the lack of purification, and we have also observed a splitting of the G-band into two peaks. The first peak, referred to as the G-peak located around ∼1590 cm^{-1}, arises due to in-plane stretching of sp^2 hybridized carbon atoms [36]. The second peak, known as the D′ peak appearing at ∼1639 cm^{-1} is commonly observed in disordered graphitic materials. This D′ peak referred to as a disorder-induced band, could potentially be a result of nitrogen doping in our specific case. The splitting could arise due to interaction of the localized vibrational modes of the dopants or impurities with extended phonon modes of graphene. Another peak at ∼2760 cm^{-1} is sometimes referred to as 2D and sometimes as G′ peak which is present due to second order (two-phonon) Raman scattering of graphitic sp^2 carbons. The shape of the 2D band being broad and consisting of two components signifies crystalline graphitic structure of our N-GQDs [34, 37, 38]. A very strong peak at 2926 cm^{-1} can be due to C–H bonds as confirmed by FTIR [39].

The XPS survey spectrum of the AP and RD N-GQDs is given in figure 5(a) and shows presence of C, N, O at 285 eV, 401 eV and 531 eV respectively for both the samples. The O atomic concentration is slightly higher for the RD N-GQDs (28 at%) compared to that of AP N-GQDs (25 at%), in agreement with the FTIR analysis that suggested oxidation due to drying in air. High resolution C 1s and N 1s spectra of the N-GQDs are given in figures 5(b) and (c). Deconvolution of the spectra reveal the presence of C=C sp^2 carbon at 284.5 eV [40], C–C/C–H sp^3 carbon at 285.1 eV [40], C-N at 285.9 eV [40], C–O at 286.4 eV [41], C=N at 287.3 eV [42, 43], C=O at 288.0 eV [41], O–C=O at 288.9 eV [44, 45], pyridinic nitrogen at 399.1 eV [41, 46], amine and amide nitrogen at 399.9 eV [40], pyrrolic nitrogen at 400.6 eV

[47] and graphitic nitrogen at 401.3 eV [47]. Pyridinic N is a substitutional type of nitrogen doping where the N atom is substituted in a six-membered carbon ring hence present in the edge-site of the N-GQDs. Amine N is present on the surface of the N-GQDs, pyrrolic N is substituted in a five-membered carbon ring and is present in the edge-site of the N-GQDs. Graphitic N is the result of core-doping which occurs as substitutional nitrogen in a six-membered carbon ring. Sometimes graphitic N can occur at the edge-site in a six-membered carbon ring where it is bonded with hydrogen atom or alkyl group [48]. AP and RD N-GQDs present very similar features and these results confirm the presence of a carbon core with both nitrogen and oxygen also included. Most of the carbon contribution in the N-GQDs is present as sp^2 and C–C/C–H bonds as we would expect for graphene layers. However, the nitrogen doping and surface oxygen-based functionalization is also observed from the deconvolution of the C 1s peak. Figure 5(c) confirms that for the most part nitrogen doping occurs in the form of graphitic nitrogen with a smaller contribution from pyridinic and pyrrolic nitrogen. The only small difference between AP and RD N-GQDs is represented by a lower contribution from the C–C/C–H bonds in the RD N-GQDs and slightly higher contributions from other bonds due to exposure to air during the re-dispersion step. Overall, our chemical analysis indicates the presence of graphene layers doped by graphitic nitrogen and functionalization at the edges by oxygen and nitrogen, with the latter only in minor part.

The absorbance spectra of AP and RD N-GQDs are given in figure 6(a). The spectra for both AP and RD samples show an onset in the visible region at about 458 nm and strong optical absorption in the UV region. High absorption close to 250 nm could be due to $\pi \to \pi^*$ transition involving aromatic sp^2 carbons and the peak at ∼330 nm can be assigned to an $n \to \pi^*$ transition involving functional groups with electron lone pairs [49–51] such as oxygen and nitrogen in our case. Reports in literature suggest that the surface functional groups play a major role in the absorption of the carbon based nanocrystals [52] and we note that the RD N-GQDs exhibit stronger absorption in the lower wavelength range. The absorption tail is reported to be due to the surface state resulting from the hybridization between the carbon core and the surface connected functional groups [53]. Direct bandgap Tauc plots for the AP and RD samples are shown in figures 6(b)–(c) and indirect bandgap in figures 6(d)–(e). When the linear region of the Tauc plot is fitted and extrapolated to the energy axis, a direct bandgap (onset of strong absorption) of 3.3 eV is obtained for both the AP and RD N-GQDs (figures 6(b)–(c)) and indirect bandgap (onset of weak absorption) of 2.9 eV is obtained for AP and RD N-GQDs (figures 6(d)–(e)). The direct bandgap in these N-GQDs is due to charge transfer by electrons from the functional groups to the carbon core and the indirect bandgap is due to the surface states [54]. Due to re-dispersion there is no difference in optical absorption and bandgap of the N-GQDs and the impact of minor oxidation on the optical properties is therefore negligible in this case.
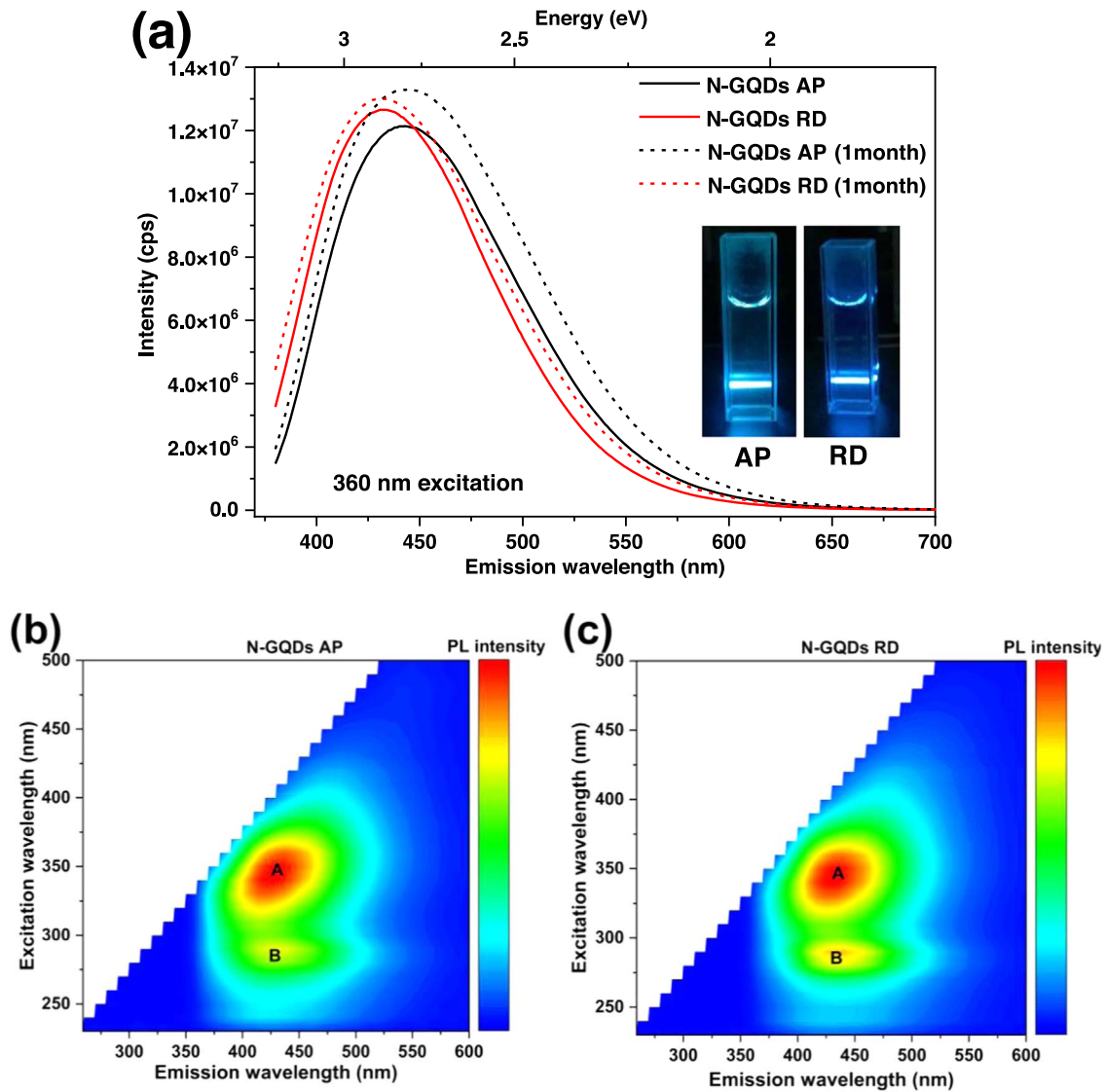
Figure 8. (a) PL spectra for as-prepared and re-dispersed samples excited with 360 nm (inset: optical photographs of AP and RD N-GQDs excited with 375 nm diode laser); Colour-coded contour maps showing the photoemission spectra of N-GQDs for (b) AP, and (c) RD sample.

To rationalize the experimental results, we calculated the absorbance spectra using time dependent density functional perturbation theory (TD-DFPT) within the simplified Tamm–Dancoff approximation (sTDA) [55], for details see the SI. We use the WB97 hybrid functional [56] and employ the def2-SV(P) basis set [57] and the corresponding Coulomb fitting bases [58]. The structures are fully relaxed, and we include an empirical dispersion correction to the total energy (forces) [59]. All grounds-state density functional theory calculations were performed using the quantum chemistry package Turbomole [54].

The GQDs are modelled as 3-layered GQD with a diameter of $d = 2.0$ nm, which corresponds to the lower end of the experimentally observed GQD size and a nitrogen concentration of ~6%. Following the FTIR based (figure 3) chemical analysis presented above we consider a fully hydrogen passivated GQD as model for the AP N-GQDs ($C_{256}N_{18}H_{72}$) and a partially oxidized GQD where we substitute hydrogen termination with amine, epoxy, and hydroxy

groups, as model for the RD N-GQDs ($C_{256}N_{24}O_{18}H_{72}$) (figure 7 inset). The calculated absorbance spectra are given in figure 7. Our calculations reproduce the features observed in experiment (figure 6(a)) and confirm that the effect of the oxidation introduced due to the redispersion of the GNDs remains indeed small in the observed energy range.

PL spectra of the N-GQDs are given in figure 8(a) for an excitation wavelength at 360 nm compared with 1 month after synthesis. Emission for both AP and RD sample is found to be in the visible region at 444 nm and 431 nm and there is no degradation in the intensity of emission after 1 month. The wavelength at which highest emission intensity occurs for 360 nm excitation is unchanged even one month after the synthesis. The photograph of the N-GQDs when excited with 375 nm diode laser is given as inset in figure 8(a) which shows visible blue emission. The excitation wavelength was varied between 230 and 500 nm and the emission spectra were measured, resulting in excitation–emission matrix (EEM) with colour-coded maps of the photoemission as given
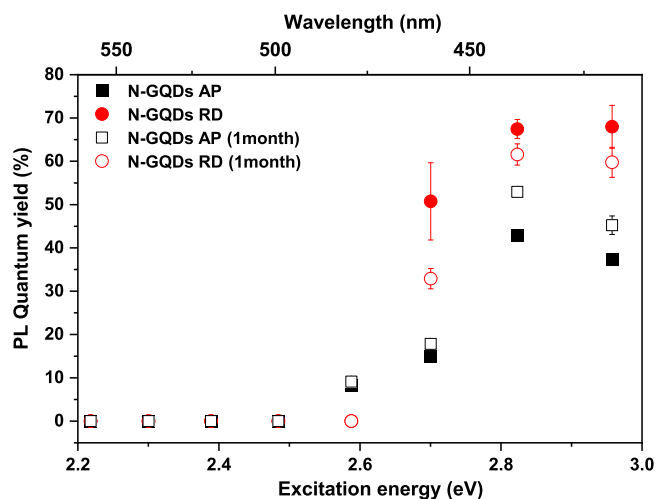
Figure 9. PL quantum yield of the AP and RD N-GQDs measured soon after synthesis and after one month (error bar shows the standard error) in colloid form.

in figures 8(b)–(c) with emission wavelength in the *x*-axis, excitation in *y*-axis and the colour scale giving the PL intensity. The emission spectra for the samples have similar features and exhibit main emission from $n \rightarrow \pi^*$ absorption (region 'A') and weak emission from the far-UV $\pi \rightarrow \pi^*$ absorption (region 'B'). The emission region A with maximum emission at 400–450 nm is excited between 320 and 370 nm. The excitation energy of region 'A' is close to the direct bandgap of these N-GQDs and the resulting emission is originating from the excitation of $n \rightarrow \pi^*$ levels. The emission could therefore be due to radiative transitions from above-bandgap energy levels to the ground state, however the emission wavelength is only weakly dependent on the excitation wavelength, and this suggests that surface/molecular states may play an important role in this case. Therefore, there might be a combined contribution of both band-to-band transitions as well as transitions localized at the surface or at the dopant sites. Emission maxima at region 'B' for the RD sample is of higher intensity compared to the AP prepared sample and possibly arises from the higher oxygen content in the RD sample due to the drying process in air.

The PL quantum yield (QY) is calculated in colloid for both AP and RD N-GQDs at a range of excitation energies. The plot of PLQY as a function of excitation energy is given in figure 9 which includes the measurement repeated one month after synthesis. The PLQY is found to increase slowly once the excitation energy is increased above 2.6 eV and reaches its maximum at ~2.8 eV. The maximum PLQY of ~68% is obtained for the RD sample at 420 nm excitation. This excitation wavelength is very close to the indirect bandgap of the N-GQDs and indicates that the most efficient radiative combination occurs when the N-GQDs are excited with energy slightly greater than the bandgap where the recombination can occur both at the band edge as well at surface/molecular states as previously discussed. While the RD N-GQDs show a slight decrease of the PLQY, the AP have increased slightly upon ageing. The high QY can be attributed to the surface groups and doping which can be altered to obtain variations in the QY. The higher PLQY for the RD samples could arise due to higher oxygen content as observed from both FTIR and XPS analysis. The reasonably high QY could be due to the graphitic structure, non-defective doping and well passivated edges as evidenced in our XPS analysis. This combined analysis indicates that the photoluminescence originates from the collective effect of nitrogen doping and oxygen functionalization of the N-GQDs. Furthermore, the PLQY increased significantly in comparison to our earlier work on N-doped carbon quantum dots (PLQY ~ 40%) [26] due to an increase of states and $n \rightarrow \pi^*$ transitions. The re-dispersion suggest that oxygen-based passivation may be an effective way to improve PLQY in carbon nanostructures and optical properties in general when combined with nitrogen doping strategies, also providing long-term stability in ambient conditions.

Conclusion

Environmentally friendly nitrogen doped graphite quantum dots have been successfully synthesized by a one-step, easy and convenient process that utilize water and simple precursors. The structural, chemical, and optical characterization supports the presence of a graphitic core structure doped with nitrogen and a functionalized surface with nitrogen- and oxygen-containing groups. Since these highly fluorescent quantum dots are stable, water dispersible and non-toxic, they have potential to be used in cellular imaging processes. The high stability and quantum yield blue luminescence arises due to radiative recombination assisted by the surface states and created by doping and oxidation, which does not impact the crystalline core structure. This room-temperature and ambient microplasma-method, without further post-synthesis treatments such as annealing or filtration methods, has allowed the synthesis of crystalline discs with a high PL quantum yield of 68%, which exceeds values in the literature that have used similar synthesis methods.

Acknowledgments

Data availability statement

All data that support the findings of this study are included within the article (and any supplementary files).

ORCID iDs

Slavia Deeksha Dsouza ⓘ https://orcid.org/0000-0001-6814-819X
Marius Buerkle ⓘ https://orcid.org/0000-0003-3464-2549
Bruno Alessi ⓘ https://orcid.org/0000-0002-4468-0381
Paul Brunet ⓘ https://orcid.org/0000-0002-0115-2976
Alessio Morelli ⓘ https://orcid.org/0000-0001-5977-0331
Amir Farokh Payam ⓘ https://orcid.org/0000-0002-6433-2261
Paul Maguire ⓘ https://orcid.org/0000-0002-2725-4647
Davide Mariotti ⓘ https://orcid.org/0000-0003-1504-4383
Vladimir Svrcek ⓘ https://orcid.org/0000-0003-0473-8363

References

[1] Tian L J *et al* 2019 Substrate metabolism-driven assembly of high-quality CdS_xSe_{1-x} quantum dots in *Escherichia coli*: molecular mechanisms and bioimaging application *ACS Nano* **13** 5841–51

[2] Li H, Bian Y, Zhang W, Wu Z, Ahn T K, Shen H and Du Z 2022 High performance InP-based quantum dot light-emitting diodes via the suppression of field-enhanced electron delocalization *Adv. Funct. Mater.* **32** 2204529

[3] Zhang W *et al* 2023 Nano-carrier for gene delivery and bioimaging based on pentaetheylenehexamine modified carbon dots *J. Colloid Interface Sci.* **639** 180–92

[4] Soheyli E, Azad D, Sahraei R, Hatamnia A A, Rostamzad A and Alinazari M 2019 Synthesis and optimization of emission characteristics of water-dispersible ag-in-s quantum dots and their bactericidal activity *Colloids Surf.*B **182** 110389

[5] Wang Q, Xu Y, Zhang L, Niu P, Zhou R, Lyu M, Lu H and Zhu J 2022 Aromatic carboxylic acid ligand management for $CsPbBr_3$ quantum dot light-emitting solar cells *ACS Appl. Nano Mater.* **5** 10495–503

[6] Lin L, Rong M, Luo F, Chen D, Wang Y and Chen X 2014 Luminescent graphene quantum dots as new fluorescent materials for environmental and biological applications *TrAC - Trends Anal. Chem.* **54** 83–102

[7] Xu X, Ray R, Gu Y, Ploehn H J, Gearheart L, Raker K and Scrivens W A 2004 Electrophoretic analysis and purification of fluorescent single-walled carbon nanotube fragments *J. Am. Chem. Soc.* **126** 12736–7

[8] Mansuriya B D and Altintas Z 2021 Carbon dots: classification, properties, synthesis, characterization, and applications in health care-an updated review (2018–2021) *Nanomaterials* **11** 2525

[9] Đorđević L, Arcudi F, Cacioppo M and Prato M 2022 A multifunctional chemical toolbox to engineer carbon dots for biomedical and energy applications *Nat. Nanotechnol.* **17** 112–30

[10] Ren J, Malfatti L and Innocenzi P 2021 Citric acid derived carbon dots, the challenge of understanding the synthesis-structure relationship *J. Carbon Res.* **7** 2

[11] Xu Y, Wu M, Liu Y, Feng X Z, Yin X B, He X W and Zhang Y K 2013 Nitrogen-doped carbon dots: a facile and general preparation method, photoluminescence investigation, and imaging applications *Chem. - A Eur. J.* **19** 2276–83

[12] Wang X, Cao L, Yang S-T, Lu F, Meziani M J, Tian L, Sun K W, Bloodgood M A and Sun Y-P 2010 Bandgap-like strong fluorescence in functionalized carbon nanoparticles *Angew* **49** 5310–4

[13] Das A, Roy D, Mandal M, Jaiswal C, Ta M and Mandal P K 2018 Carbon dot with pH independent near-unity photoluminescence quantum yield in an aqueous medium: electrostatics-induced förster resonance energy transfer at submicromolar concentration *J. Phys. Chem. Lett.* **9** 5092–9

[14] Zhang Y, Liu X, Fan Y, Guo X, Zhou L, Lv Y and Lin J 2016 One-step microwave synthesis of N-doped hydroxyl-functionalized carbon dots with ultra-high fluorescence quantum yields *Nanoscale* **8** 15281–7

[15] Zheng C, An X and Gong J 2015 Novel pH sensitive N-doped carbon dots with both long fluorescence lifetime and high quantum yield *RSC Adv.* **5** 32319–22

[16] Mura S, Ludmerczki R, Stagi L, Garroni S, Carbonaro C M, Ricci P C, Casula M F, Malfatti L and Innocenzi P 2020 Integrating sol-gel and carbon dots chemistry for the fabrication of fluorescent hybrid organic-inorganic films *Sci. Rep.* **10** 4770

[17] Qu D, Zheng M, Zhang L, Zhao H, Xie Z, Jing X, Haddad R E, Fan H and Sun Z 2014 Formation mechanism and optimization of highly luminescent N-doped graphene quantum dots *Sci. Rep.* **4** 5294

[18] Talite M J, Huang H Y, Bin Cai K, Capinig Co K C, Cynthia Santoso P A, Chang S H, Chou W C and Yuan C T 2020 Visible-transparent luminescent solar concentrators based on carbon nanodots in the siloxane matrix with ultrahigh quantum yields and optical transparency at high-loading contents *J. Phys. Chem. Lett.* **11** 567–73

[19] Yuan T, Yuan F, Sui L, Zhang Y, Li Y, Li X, Tan Z and Fan L 2023 Carbon quantum dots with near-unity quantum yield bandgap emission for electroluminescent light-emitting diodes *Angew. Chem.* **135** e202218568

[20] Guo J, Lu Y, Xie A Q, Li G, Bin Liang Z, Wang cf, Yang X and Chen S 2022 Yellow-emissive carbon dots with high solid-state photoluminescence *Adv. Funct. Mater.* **32** 2110393

[21] Mariotti D, Belmonte T, Benedikt J, Velusamy T, Jain G and Svrcek V 2016 Low-temperature atmospheric pressure plasma processes for 'Green' third generation photovoltaics *Plasma Process. Polym.* **13** 70–90

[22] Mariotti D and Sankaran R M 2010 Microplasmas for nanomaterials synthesis *J. Phys. D: Appl. Phys.* **43** 323001–21

[23] Ma X, Li S, Hessel V, Lin L, Meskers S and Gallucci F 2019 Synthesis of luminescent carbon quantum dots by microplasma process *Chem. Eng. Process. - Process Intensif.* **140** 29–35

[24] Huang X, Li Y, Zhong X, Rider A E and Ostrikov K 2015 Fast microplasma synthesis of blue luminescent carbon quantum dots at ambient conditions *Plasma Process. Polym.* **12** 59–65

[25] Carolan D, Rocks C, Padmanaban D B, Maguire P, Svrcek V and Mariotti D 2017 Environmentally friendly nitrogen-doped carbon quantum dots for next generation solar cells *Sustain. Energy Fuels* **1** 1611–9

[26] Dsouza S D, Buerkle M, Brunet P, Maddi C, Padmanaban D B, Morelli A, Payam A F, Maguire P, Mariotti D and Svrcek V 2021 The importance of surface states in N-doped carbon quantum dots *Carbon N.Y.* **183** 1–11

[27] Wang J, Zhang P, Huang C, Liu G, Leung Kcf and Wáng Y X J 2015 High performance photoluminescent carbon dots for *in vitro* and *in vivo* bioimaging: effect of nitrogen doping ratios *Langmuir* **31** 8063–73

[28] Carbonaro C M, Corpino R, Salis M, Mocci F, Thakkar S V, Olla C and Ricci P C 2019 On the emission properties of carbon dots: reviewing data and discussing models *C. J. Carbon Res.* **5** 60

[29] Li Y, Zhong X, Rider A E, Furman S A and Ostrikov K 2014 Fast, energy-efficient synthesis of luminescent carbon quantum dots *Green Chem.* **16** 2566–70

[30] Mitra T, Sailakshmi G, Gnanamani A and Mandal A B 2013 Studies on cross-linking of succinic acid with chitosan/collagen *Mater. Res.* **16** 755–65

[31] Dong Y, Shao J, Chen C, Li H, Wang R, Chi Y, Lin X and Chen G 2012 Blue luminescent graphene quantum dots and graphene oxide prepared by tuning the carbonization degree of citric acid *Carbon N.Y.* **50** 4738–43

[32] Mallamace F, Corsaro C, Mallamace D, Vasi S, Vasi C and Dugo G 2015 The role of water in protein's behavior: the two dynamical crossovers studied by NMR and FTIR techniques *Comput. Struct. Biotechnol. J.* **13** 33–7

[33] Dervishi E, Ji Z, Htoon H, Sykora M and Doorn S K 2019 Raman spectroscopy of bottom-up synthesized graphene quantum dots: size and structure dependence *Nanoscale* **11** 16571–81

[34] Jorio A, Saito R, Dresselhaus G and Dresselhaus M S 2011 *Raman Spectroscopy in Graphene Related Systems* (Germany: Wiley) (https://doi.org/10.1002/9783527632695)

[35] Liu D *et al* 2018 Raman enhancement on ultra-clean graphene quantum dots produced by quasi-equilibrium plasma-enhanced chemical vapor deposition *Nat. Commun.* **9** 193

[36] Kouloumpis A, Thomou E, Chalmpes N, Dimos K, Spyrou K, Bourlinos A B, Koutselas I, Gournis D and Rudolf P 2017 Graphene/carbon dot hybrid thin films prepared by a modified langmuir-schaefer method *ACS Omega* **2** 2090–9

[37] Raja P M V and Barron A R 2019 *Physical Methods in Chemistry and Nano Science* (Rice University: OpenStax CNX) (https://hdl.handle.net/1911/112293)

[38] Ferrari A C *et al* 2006 Raman spectrum of graphene and graphene layers *Phys. Rev. Lett.* **97** 187401

[39] Miranda A M, Castilho-Almeida E W, Martins Ferreira E H, Moreira G F, Achete C A, Armond R A S Z, Dos Santos H F and Jorio A 2014 Line shape analysis of the Raman spectra from pure and mixed biofuels esters compounds *Fuel* **115** 118–25

[40] Arcudi F, Dordevic L and Prato M 2016 Synthesis, separation, and characterization of small and highly fluorescent nitrogen-doped carbon nanodots *Angew. Chemie - Int. Ed.* **55** 2107–12

[41] Tang L, Ji R, Li X, Teng K S and Lau S P 2013 Energy-level structure of nitrogen-doped graphene quantum dots *J. Mater. Chem.*C **1** 4908–15

[42] Daems N, Sheng X, Vankelecom I F J and Pescarmona P P 2014 Metal-free doped carbon materials as electrocatalysts for the oxygen reduction reaction *J. Mater. Chem.*A **2** 4085–110

[43] Schneider J, Reckmeier C J, Xiong Y, Von Seckendorff M, Susha A S, Kasak P and Rogach A L 2017 Molecular fluorescence in citric acid-based carbon dots *J. Phys. Chem.* C **121** 2014–22

[44] Liu X, Han J, Hou X, Altincicek F, Oncel N, Pierce D, Wu X and Zhao J X 2021 One-pot synthesis of graphene quantum dots using humic acid and its application for copper (II) ion detection *J. Mater. Sci.* **56** 4991–5005

[45] Qian L, Thiruppathi A R, Elmahdy R, van der Zalm J and Chen A 2020 Graphene-oxide-based electrochemical sensors for the sensitive detection of pharmaceutical drug naproxen *Sensors* **20** 1252

[46] Liu H, Li Z, Sun Y, Geng X, Hu Y, Meng H, Ge J and Qu L 2018 Synthesis of Luminescent carbon dots with ultrahigh quantum yield and inherent folate receptor-positive cancer cell targetability *Sci. Rep.* **8** 1–8

[47] Wang H, Maiyalagan T and Wang X 2012 Review on recent progress in nitrogen-doped graphene: synthesis, characterization, and its potential applications *ACS Catal.* **2** 781–94

[48] Sarkar S, Sudolská M, Dubecký M, Reckmeier C J, Rogach A L, Zbořil R and Otyepka M 2016 Graphitic nitrogen doping in carbon dots causes red-shifted absorption *J. Phys. Chem.*C **120** 1303–8

[49] Zhu S, Song Y, Zhao X, Shao J, Zhang J and Yang B 2015 The photoluminescence mechanism in carbon dots (graphene quantum dots, carbon nanodots, and polymer dots): current state and future perspective *Nano Res.* **8** 355–81

[50] Park Y, Yoo J, Lim B, Kwon W and Rhee S-W 2016 Improving the functionality of carbon nanodots: doping and surface functionalization *J. Mater. Chem.*A **4** 11582–603

[51] Luo Z, Lu Y, Somers L A and Johnson A T C 2009 High yield preparation of macroscopic graphene oxide membranes high yield preparation of macroscopic graphene oxide membranes *J. Am. Chem. Soc.* **131** 898–9

[52] Roy P, Chen P C, Periasamy A P, Chen Y N and Chang H T 2015 Photoluminescent carbon nanodots: synthesis, physicochemical properties and analytical applications *Mater. Today* **18** 447–58

[53] Zhu S, Song Y, Wang J, Wan H, Zhang Y, Ning Y and Yang B 2017 Photoluminescence mechanism in graphene quantum dots: quantum confinement effect and surface/edge state *Nano Today* **13** 10–4

[54] Turbomole v7.0 2015 *2015 Package For Electronic Structure Calculations Features at a Glance* (Turbomole GmbH) (www.turbomole.com)

[55] Grimme S 2013 A simplified Tamm-Dancoff density functional approach for the electronic excitation spectra of very large molecules *J. Chem. Phys.* **138** 244104

[56] Da Chai J and Head-Gordon M 2008 Systematic optimization of long-range corrected hybrid density functionals *J. Chem. Phys.* **128** 084106

[57] Weigend F and Ahlrichs R 2005 Balanced basis sets of split valence, triple zeta valence and quadruple zeta valence quality for H to Rn: design and assessment of accuracy *Phys. Chem. Chem. Phys.* **7** 3297–305

[58] Weigend F 2006 Accurate Coulomb-fitting basis sets for H to Rn *Phys. Chem. Chem. Phys.* **8** 1057–65

[59] Caldeweyher E, Mewes J M, Ehlert S and Grimme S 2020 Extension and evaluation of the D4 London-dispersion model for periodic systems *Phys. Chem. Chem. Phys.* **22** 8499–512